

LOW ANGULAR MOMENTUM IN CLUMPY, TURBULENT DISK GALAXIES

DANAIL OBRESCHKOW¹, KARL GLAZEBROOK², ROBERT BASSETT², DAVID B. FISHER², ROBERTO G. ABRAHAM³, EMILY WISNIOSKI⁴, ANDREW W. GREEN⁵, PETER J. MCGREGOR⁶, IVANA DAMJANOV⁷, ATTILA POPPING^{1,8} & INGER JØRGENSEN⁹

¹International Centre for Radio Astronomy Research, Uni. of Western Australia, 7 Fairway, Crawley, WA 6009, Australia; ²Centre for Astrophysics & Supercomputing, Swinburne Uni. of Technology, PO Box 218, Hawthorn, VIC 3122, Australia; ³Department of Astronomy and Astrophysics, Uni. of Toronto, 50 St George St, Toronto, ON M5S3H4, Canada; ⁴Max Planck Institut für extraterrestrische Physik, Postfach 1312, Giessenbachstr., D-85741 Garching, Germany; ⁵Australian Astronomical Observatory, PO Box 915, North Ryde, NSW 1670, Australia; ⁶Research School of Astronomy and Astrophysics, Australian National Uni., Cotter Rd, Weston, ACT 2611, Australia; ⁷Harvard-Smithsonian CfA, 60 Garden St., MS-20, Cambridge, MA 02138, USA; ⁸ARC Centre of Excellence for All-sky Astrophysics (CAASTRO); ⁹Gemini Observatory, 670 N. A'ohoku Pl., Hilo, HI 96720, USA

Draft version March 2, 2022

ABSTRACT

We measure the stellar specific angular momentum $j_s = J_s/M_s$ in four nearby ($z \approx 0.1$) disk galaxies that have stellar masses M_s near the break M_s^* of the galaxy mass function, but look like typical star-forming disks at $z \approx 2$ in terms of their low stability ($Q \approx 1$), clumpiness, high ionized gas dispersion ($40\text{--}50 \text{ km s}^{-1}$), high molecular gas fraction (20–30%) and rapid star formation ($\sim 20 \text{ M}_\odot \text{ yr}^{-1}$). Combining high-resolution (Keck-OSIRIS) and large-radius (Gemini-GMOS) spectroscopic maps, only available at low z , we discover that these targets have ~ 3 times less stellar angular momentum than typical local spiral galaxies of equal stellar mass and bulge fraction. Theoretical considerations show that this deficiency in angular momentum is the main cause of their low stability, while the high gas fraction plays a complementary role. Interestingly, the low j_s values of our targets are similar to those expected in the M_s^* -population at higher z from the approximate theoretical scaling $j_s \propto (1+z)^{-1/2}$ at fixed M_s . This suggests that a change in angular momentum, driven by cosmic expansion, is the main cause for the remarkable difference between clumpy M_s^* -disks at high z (which likely evolve into early-type galaxies) and mass-matched local spirals.

1. INTRODUCTION AND MOTIVATION

In studying the history of the universe, the galaxy population that contributes most of the star formation density at a given epoch is of central interest. Individual galaxies can evolve into and out of this population, but remarkably the dominant star-forming population itself always remains composed of disks with similar stellar masses of $M_s = 10^{10}\text{--}10^{11} \text{ M}_\odot$, at redshifts $z < 3$ (Karim et al. 2011). This mass range coincides with the ‘knee’ in the mass function of star-forming galaxies, centered at $M_s^* = 10^{10.7}\text{--}10^{11} \text{ M}_\odot$ at $z < 3$ (Muzzin et al. 2013).

Although the dominant star-forming population always consists of M_s^* -galaxies of similar mass, the nature of these galaxies changes significantly with z . In modern times ($z \approx 0$), most of these galaxies are stable spiral disks like the Milky Way. They have low velocity dispersion and balance gravity almost entirely by rotation. Stars form at modest rates ($\sim 1 \text{ M}_\odot \text{ yr}^{-1}$) in thousands of clouds with individual masses around $10^5\text{--}10^6 \text{ M}_\odot$ (Murray 2011). In contrast, galaxies of the same mass in past epochs ($z \approx 1\text{--}3$) form stars 10–100 times more rapidly. Most of this fast star formation occurs in giant gas clumps of $10^8\text{--}10^9 \text{ M}_\odot$ (Elmegreen & Elmegreen 2005), reminiscent of merging proto-galaxies, but now interpreted as large Jeans instabilities (Bournaud et al. 2007). These disks are rich in turbulent gas (Genzel et al. 2008) and yield marginal rotational support and stability (Förster Schreiber et al. 2006). Because of mass growth, these clumpy M_s^* -disks at $z \approx 2$ are likely to evolve into early-type galaxies (ETGs, Tacchella et al. 2015).

The stark morpho-dynamical difference between early and modern star-forming galaxies, in spite of identi-

cal masses, raises the question as to how these galaxies ‘know’ what cosmic time they are at. Is their difference explained by a change in the mass composition, such as the established decline in the cold gas fraction (Tacconi et al. 2010) and the molecular-to-atomic ratio (Obreschkow & Rawlings 2009), or are these paralleled by a more fundamental driver? Angular momentum is a promising contender because of its predicted z -dependence at fixed galaxy mass: the stellar specific angular momentum $j_s \equiv J_s/M_s$ is expected to scale as $j_s \propto (1+z)^{-1/2}$ for fixed stellar mass M_s (not individual galaxies) as discussed in Section 3.1. This motivates the question whether low angular momentum drives or contributes to the marginal stability of the clumpy, turbulent M_s^* -disks commonly found at high z . This idea is further stimulated by the empirical fact that j_s is also the dominant driver of morphological differences in regular galaxies of equal mass at $z \approx 0$ (Romanowsky & Fall 2012; Obreschkow & Glazebrook 2014).

Direct angular momentum measurements of clumpy, turbulent disks at $z > 1$ are, however, challenged by difficulties of conducting deep, high-resolution spectroscopic observations at such large cosmic distances. Overcoming this challenge was the motivation to assemble the ‘DYNAMO’ galaxies (Green et al. 2014), a sample of 95 galaxies containing some of the most H α luminous ($L_{\text{H}\alpha} > 10^{42} \text{ erg s}^{-1}$) nearby ($z \approx 0.1$) galaxies, excluding AGN, in the Sloan Digital Sky Survey (York et al. 2000). Follow-up observations (Section 2) revealed that, merging objects aside, the H α luminous DYNAMO objects are analogous to typical clumpy disks at $z \approx 1\text{--}3$ (details in Section 2). Hence, the DYNAMO sample is an interest-

ing laboratory to probe the angular momenta in clumpy galaxies, normally too distant for such measurements.

The objective of this article is to answer two questions: (i) what role does angular momentum play in shaping the rare clumpy, turbulent disks at low- z , and (ii) what can these low- z studies tell us about the high- z star-forming population? These questions will be examined using a pilot sample of four clumpy DYNAMO disks with exquisite integral field spectroscopy (IFS) data. Section 2 describes the sample and summarizes the kinematic measurements, expanded in the Appendix. Section 3 discusses and interprets the results, synthesized in Section 4.

2. SAMPLE AND ANALYSIS

We perform the angular momentum measurements in a pilot sample of four DYNAMO galaxies at $z \approx 0.1$ (Figure 1 and Table 1), which exhibit H α luminosities in the top 0.1% at their redshifts, but have regular rotation and do *not* show the typical merger/starburst signatures of Ultra Luminous Infrared Galaxies. The targets have stellar masses near M_s^* , similar to the Milky Way ($\log(M_s/M_\odot) = 10.8$, McMillan 2011), but appear to be highly reminiscent of typical star-forming galaxies at $z \approx 2$ given the following properties: (i) they are composed of giant star-forming clumps revealed in HST H α -imaging (Bassett et al. 2014), (ii) they exhibit high star formation rates (mean of $20 \text{ M}_\odot \text{ yr}^{-1}$) comparable to main-sequence galaxies at $z \geq 1$ (Green et al. 2014), (iii) they have turbulent (flux weighted gas dispersion $\sigma = 40\text{--}50 \text{ km s}^{-1}$), but rotationally supported disks ($V/\sigma = 3\text{--}5$) placed on a Tully-Fisher relation (Green et al.), (iv) the disk sizes ($R_e \approx 3 \text{ kpc}$) are comparable to those of M_s^* -disks at $z \geq 1$ (Green et al.), (v) CO(1–0) emission data uncovers high molecular gas fractions (20–30%, Fisher et al. 2014).

Given the strong analogy to high- z turbulent disk galaxies, our objects represent an exquisite laboratory for studying such clumpy disks at distances 20-times closer than possible so far. To our knowledge, the DYNAMO sample is unique in that it fulfils *all* the above properties, including $M_s \approx M_s^*$. Therefore, our sample is a useful addition to the well-established class of ‘low- z analogs of high- z objects’, reviewed by Glazebrook (2013) and Elmegreen et al. (2013).

Our measurements of j_s (details in Appendix A & B) rely on high-resolution adaptive optics IFS data from Keck-OSIRIS to probe the inner parts and, in two objects (G04-1 and G20-2), natural seeing Gemini-GMOS IFS to probe the faint outer parts to $2.5R_e$. These data give, in each pixel, stellar surface densities from the broadband infrared/optical continuum and line-of-sight velocities from Doppler-shifted hydrogen emission lines (Pa α and H β). In the case of G04-1 and G20-2, we were also able to extract stellar absorption line maps, revealing that the velocities *and* dispersions of the stars are consistent with those of the ionized gas (Bassett et al. 2014). We can therefore adopt a single rotation curve for gas and stars. Where available, data from both spectrographs is combined (Appendix A). We note that the OSIRIS data confirms the high velocity dispersion found by Green et al. (2014) ($45\text{--}50 \text{ km s}^{-1}$ for G04-1, G20-2) at a high spatial resolution where the effect of beam smearing is negligible (Oliva et al. in prep.).

Kinematic models are fitted *simultaneously* to the com-

bined continuum-density and emission line-velocity data, making no assumption on the rotation structure other than circular rotation in a disk (Appendix B). The fitting routine was successfully verified against degraded mock data of 1,000 model-galaxies and the control galaxy NGC 3198 (see Appendix C).

The fits to all targets (Figure 1) are excellent in that no global (mono-, di-, or quadrupole) systematics can be seen in the density and velocity residuals. Table 1 lists the fitting parameters and two values for j_s , one ($j_{s,\text{obs}}$) based on the pixels that have IFS data, and one ($j_{s,\text{tot}}$) that also includes an extrapolation to infinite radii assuming an asymptotically flat rotation and exponential disk for the outer regions without data. For the two galaxies with only inner rotation data, to one effective radius R_e , from Keck-OSIRIS, the fraction of the total specific angular momentum $j_{s,\text{tot}}$ that is extrapolated is about 60%, and the estimated statistical uncertainty of $j_{s,\text{tot}}$ amounts to about 18%. In the two galaxies with additional natural seeing Gemini-GMOS data, reaching beyond $2R_e$, only about 25% of $j_{s,\text{tot}}$ is extrapolated and hence the uncertainty of $j_{s,\text{tot}}$ reduces to about 11%. This shows the utility of such deep IFS data for measuring angular momentum.

In Figure 2, we compare the angular momenta of the clumpy targets to typical spiral galaxies at $z \approx 0$ in the mass-spin-morphology space, spanned by $\log M_s$, $\log j_s$, and the stellar bulge-to-total mass ratio B/T . The regular spiral galaxies of The HI Nearby Galaxy Survey (THINGS, Walter et al. 2008) lie near a plane in this space (Obreschkow & Glazebrook 2014). In these data, the bulge masses in the B/T ratios were defined as the central excess above an exponential density profile (Appendix A of Obreschkow & Glazebrook), irrespective of the bulge types (mostly pseudo-bulges). The B/T values of our four targets were computed in the same way from radial density profiles, extracted from HST r -band (filter FR647M) images (for D13-5, G04-1, G20-2) and OSIRIS K -band continuum maps (for C22-2).

For consistency, all stellar masses in Figure 2 were estimated from K -band magnitudes¹ within infinite apertures², using a small empirical k -correction (Glazebrook et al. 1995) and a universal K -band mass-to-light ratio³ $M/L_K = 0.5 \text{ M}_\odot/L_\odot$. Using a color-dependent M/L_K is more adequate in studies including galaxies with significant classical bulges that tend to be redder (Fall & Romanowsky 2013). However, in the present comparison a constant M/L_K suffices: the THINGS and DYNAMO galaxies are disk-dominated and their continuum maps are consistent with pseudo-bulges (Kormendy & Fisher 2008), except for three THINGS objects with small classical bulges. Overall, the DYNAMO galaxies tend to be bluer than typical spirals, but the M/L_K ratio is insensitive (to $< 20\%$) to this (Bell et al. 2003).

¹ K -magnitudes (Vega zero-point) are from 2MASS for DYNAMO and from $3.6\mu\text{m}$ Spitzer maps with a 2MASS-calibrated $3.6\mu\text{m}$ -to- K conversion for THINGS (Leroy et al. 2008).

² For DYNAMO objects, the 2MASS aperture is ~ 4 scale radii containing 99% of the light. For THINGS, the stellar masses in (Leroy et al. 2008) were calculated using apertures of $1.5r_{25}$. By extending the aperture to $\gtrsim 5R_e$, we find the flux to increase by a factor 1.2. This factor was applied to all THINGS galaxies.

³ Assuming a Kroupa (2001) Initial Mass Function (IMF) for consistency with the THINGS data (Leroy et al. 2008).

Table 1
Properties of the four clumpy target galaxies and the control galaxy NGC 3198.

Object	Basic properties			IFS Resolution ^c		Fitted in this work ^d							
	Redshift	M_s^a log(M_\odot)	$L_{H\alpha}^b$ log(erg s ⁻¹)	OSIRIS kpc	GMOS kpc	η deg	α deg	B/T	R_e kpc	r_{flat} kpc	v_{flat} km s ⁻¹	$j_{s,\text{obs}}$ kpc km s ⁻¹	$j_{s,\text{tot}}$ kpc km s ⁻¹
C22-2	0.07116	10.4	41.68	0.33	–	50	145	0.12	2.6	–	–	120	273 ± 49
D13-5	0.07535	10.7	42.10	0.35	–	38	127	0.01	3.5	0.5	202	356	828 ± 143
G04-1	0.12981	11.1	42.36	0.57	1.19	40	359	0.15	5.1	0.5	135	515	834 ± 116
G20-2	0.14113	10.7	42.26	0.62	1.28	46	187	0.18	2.7	0.6	118	337	394 ± 32
NGC 3198	662 km s ⁻¹	10.2		0.02	–	69	215	0.00	6.2	3.9	163	626	973 ± 122
(reference)						72 ^e	215 ^e	0.03 ^f		2.8 ^e	150 ^e		936 ± 20 ^f

Notes. ^a K -band based stellar masses ($\Upsilon_K = 0.5 M_\odot/L_\odot$); ^b $H\alpha$ luminosity as measured by IFS observations on the AAT/SPIRAL (Green et al. 2014); ^c FWHM of PSF; ^d Parameters fitted as described in Appendix B; ^e Table 4 of Leroy et al. (2008); ^f Table 1 of Obreschkow & Glazebrook (2014).

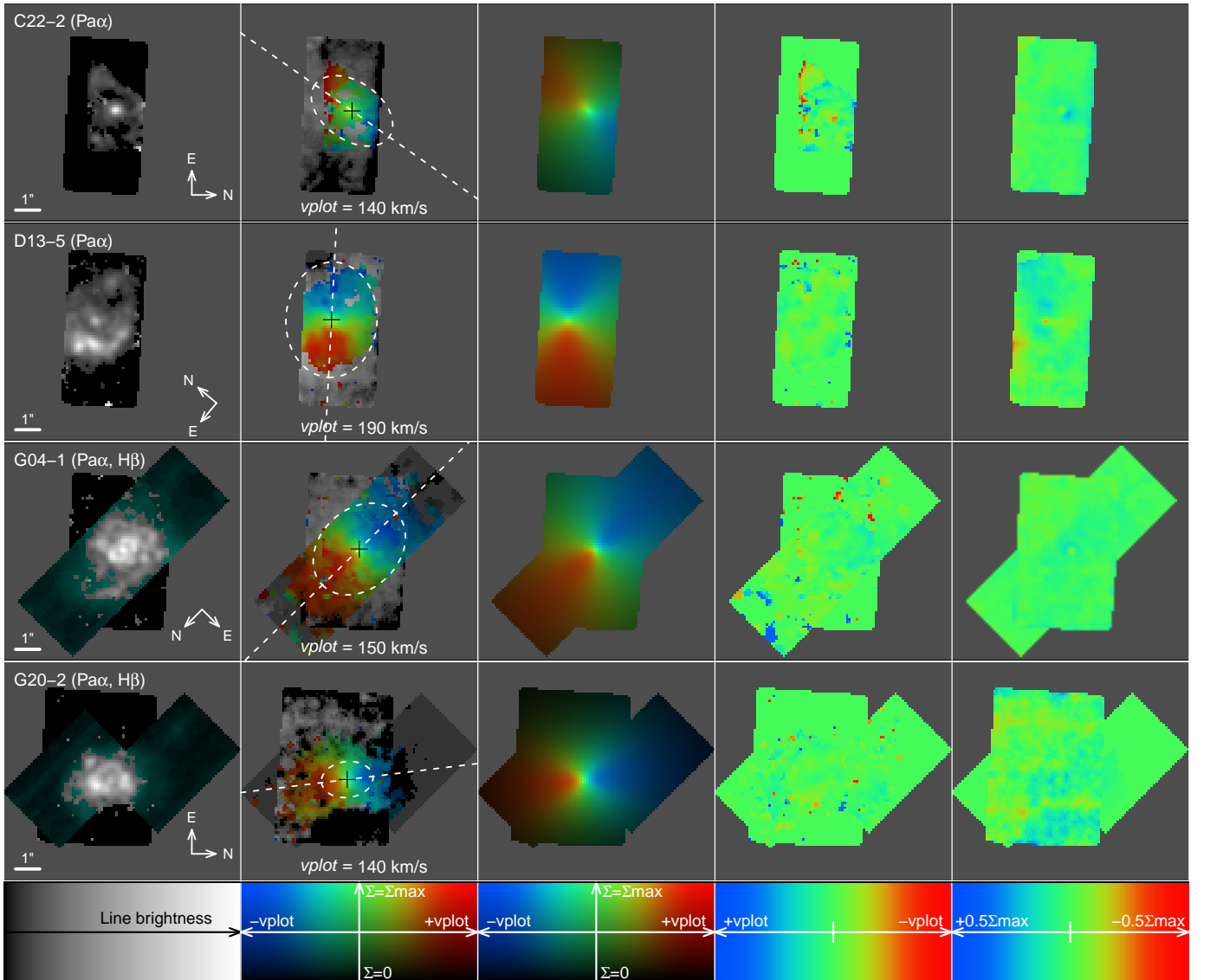


Figure 1. Kinematic fits for the four clumpy targets. Col 1: emission line fluxes of the Pa α (OSIRIS) and H β (GMOS) lines, as indicated in parentheses; H β is shown in cyan for distinction from Pa α . Cols 2&3: density+velocity maps of data and models, respectively. Lightness represents the continuum surface brightness and hue represents the rest-frame line-of-sight velocity of the emission lines. A greyscale is used where only continuum data is available. White dashed lines show the best-fit major axes and half-mass ellipses. Cols 4&5: Maps of the line-of-sight velocity residuals $\Delta v' = v' - v'_{\text{model}}$ and stellar density residuals $\Delta \Sigma_s = \Sigma_s - \Sigma_{\text{model},s}$.

3. RESULTS AND DISCUSSION

3.1. Low j_s in clumpy galaxies at $z \approx 0$

Figure 2 reveals a clear offset of the DYNAMO targets from the THINGS galaxies, corresponding to a factor 3.0 ± 0.7 shift in j_s : the clumpy targets have three times less angular momentum than regular local spiral galaxies of comparable M_s and B/T . A likelihood analysis (using the *Hyper-Fit* package of Robotham & Obreschkow 2015), accounting for the statistical uncertainties and small number statistics, shows that the offset between the two samples is certain at 5.1 standard deviations and larger than a factor 2 in j_s with 97% probability.

The immediate suggestion of Figure 2 is that the difference between turbulent, clumpy disks and regular spiral disks is in some sense related to angular momentum. The question then becomes one of causality: is the *leading* mechanism that (i) low angular momentum causes clumps, (ii) clumps cause low angular momentum, or (iii) a third quantity causes both? Options (ii) and (iii) are hard to substantiate in light of angular momentum being a conserved quantity that cannot be generated from within the galaxy-halo system. Thus, option (iii) would mean that external torques somehow cause the giant clumps while also reducing the angular momentum – an implausible scenario given that our targets show no global kinematic asymmetries hinting at such torques. For option (ii) to work, the star-forming clumps would need to drive a mechanism (e.g. via tidal torques or ejected material) for transferring angular momentum from the disk to the dark halo. However, in modern high-resolution simulations (Genel & et al. 2015) star-forming regions preferentially remove low- j gas via supernova-winds, increasing the angular momentum of the disk rather than reducing it, in order to make simulated disk galaxies as large as observed. In contrast, option (i), i.e. low- j causing clumps, appears plausible from the following fundamental stability considerations.

The stability of a galactic disk against clump formation can be quantified by the dimensionless Toomre parameter (Toomre 1964)⁴

$$Q = \frac{\sigma \kappa}{3.36 G \Sigma}, \quad (1)$$

which depends on the local surface density Σ , radial velocity dispersion σ , and epicyclic frequency κ . If $Q < 1$, instabilities can develop with diameters larger than the Jeans length L_J and smaller than the maximal stability scale L_R set by the differential rotation. If $Q > 1$, then $L_J > L_R$ and no instability can develop: all Jeans modes are stabilised by the local centrifugal acceleration.

In most galactic disks, the surface density and epicyclic frequency decrease similarly with radius, such that Q is constant within 20% (for individual galaxies, Westfall et al. 2014) across the regions that hold most of the stellar mass (at ~ 1 exponential radius) and angular momentum (at ~ 2 exponential radii). Within this level of accuracy it is therefore possible to introduce a mean Toomre parameter \bar{Q} , defined such that $\bar{Q} > 1$ corresponds to globally stable disks. The global stability parameter \bar{Q} can be rewritten as $\bar{Q} \propto M^{-1} j \sigma$ upon expressing the means of Σ and κ by the total mass M and specific an-

gular momentum j of the disk (details in Obreschkow & Glazebrook 2014). This straightforward substitution does *not* change the underlying physics, but introduces a new viewpoint, describing the disk stability in terms of fundamental quantities, conserved in isolation. As we shall see, this viewpoint allows us to link the disk stability to a time-dependent cosmological context.

So far, \bar{Q} describes the stability of a single component (stellar or gas) disk. To about 20% accuracy (Romeo & Wiegert 2011) this quantity can be extended to a multi-component (stars and gas) disk via (Wang & Silk 1994)

$$\bar{Q}^{-1} = \bar{Q}_s^{-1} + \bar{Q}_g^{-1}, \quad (2)$$

where $\bar{Q}_s \propto M_s^{-1} j_s \sigma_s$ and $\bar{Q}_g \propto M_g^{-1} j_g \sigma_g$ are the partial stability terms of the stars and cold gas, respectively. Relying on the observational finding (see §2 and Bassett et al. 2014) that stars and gas exhibit comparable velocity and dispersion maps, we here adopt the equalities $j_s = j_g \equiv j$ and $\sigma_s = \sigma_g \equiv \sigma$. This does not necessarily imply that the gas and stars develop similar instabilities, as discussed at the end of §3.1.

Introducing the gas fraction $f_g \equiv M_g/(M_s + M_g)$, the global Toomre parameter then reduces to

$$\bar{Q} \propto M_s^{-1} (1 - f_g) j_s \sigma. \quad (3)$$

Main-sequence spiral galaxies in the local universe are stable systems with $\bar{Q} \approx \bar{Q}_{\text{local}} = 2$ (Westfall et al. 2014).

We now discuss how \bar{Q} changes relative to \bar{Q}_{local} in the case of our clumpy turbulent disks. Equation (3) shows that the high velocity dispersion σ of our targets, which has about twice the amplitude of typical local disks (Andersen et al. 2006), would by itself *increase* the stability by a factor 2. The reason is that L_J increases with σ , a situation that is also observed in many high- z disks (Genzel et al. 2008). Thus, the high σ can explain the large Jeans scale (Fisher *et al.*, forthcoming), but it cannot simultaneously explain why the stability of the disks is low enough (i.e. L_R is high enough) for the Jeans modes to become manifest. Following Equation (3), this low stability despite high σ requires high gas fractions or low angular momentum (at fixed M_s). Our targets have both: $f_g = 20\text{--}30\%$ (seen in CO emission⁵) is a factor 2–3 above the typical 10% value of local M_s^* -disks (Leroy et al. 2008), while the j_s values measured in this work are a factor ~ 3 lower than in typical local M_s^* -disks.

Importantly, Equation (3) shows that the factor 1/3 reduction in j_s has a much larger direct effect on reducing \bar{Q} than the factor 2–3 increase in f_g . Thus, *low angular momentum is the dominant driver for the low stability of our targets* – the main result of this study. Quantitatively, the \bar{Q} -values of our targets are about half those of typical local spirals, due to the combination of a factor 0.8 decrease in $(1 - f_g)$, a factor 0.3 decrease in j_s , and a factor 2 increase in σ , resulting in $\bar{Q} = 0.8 \times 0.3 \times 2 \times \bar{Q}_{\text{local}} \approx 1$. How this low stability feeds back onto σ , via instability-driven turbulence and stellar feedback, is a topic of current research beyond this study.

⁵ The 20–30% refer to molecular material, observed in CO emission (Fisher et al. 2014). An additional atomic (H I) component could increase these percentages, but is expected to be situated at larger radii, negligible for the stability of the stellar component, in such dense disks (Obreschkow & Rawlings 2009).

⁴ In the case of pure gas disks σ_R is commonly expressed via the sound-speed c_s , which is well-approximated by the dispersion.

It is worth discussing some potential caveats of this stability discussion. Firstly, Equation (1) relies on a purely mechanical model of a flat disk. In the case of thick disks, the constant 3.36 decreases (Peng 2001), while energy dissipation within clumps can increase this constant. In the present context, where relative changes in \bar{Q} matter more than its absolute value, these effects only appear at second order, unlikely to affect the general results. Secondly, we have omitted the fact that the stellar component is often less clumpy than the gas – a generic observation in most turbulent disks. So the question arises if this difference in stellar and gas clumpiness can be explained in the context of a single stability parameter \bar{Q} . While this question is beyond the scope of this paper, its answer probably requires a more detailed analysis of the dynamics of instabilities. For instance, the evolution of a Jeans instability depends on the adiabatic index γ of the fluid: for molecular gas ($\gamma < 4/3$), the Jeans mass decreases with increasing density and hence any proto-instability continues its collapse while fragmenting into smaller clumps. In turn, the stellar component behaves roughly like a monoatomic gas ($\gamma = 5/3$), in which the Jeans mass increases with increasing density. Hence the collapse is stopped making the stellar disk less clumpy.

3.2. Connection to the clumpy population at $z \approx 1 - 3$

Let us now turn to our second objective, the extension of the discussion to early cosmic times. While our four targets are exotic at $z \approx 0$, their high dispersion, clumpiness, star formation and gas fraction are representative of the main sequence disk population of the same stellar mass at $z \approx 1 - 3$ (Section 2), now thought to have formed more stars than merger-driven starbursts (Rodighiero et al. 2011). It is clear that the massive star formation activity ($10\text{--}100\text{ M}_\odot\text{yr}^{-1}$) of this high- z M_s^* -population must be fuelled by copious inflows of fresh gas (Dekel et al. 2009), which in turn feeds from the intergalactic medium that is $\sim 3^3 = 27$ times denser at $z \approx 2$ than today. However, we still require an explanation for the low disk stability enabling this fresh gas to turn efficiently into molecules and stars (Tacconi et al. 2010). Is the gas itself the destabilizing agent, or do these high- z M_s^* -disks exhibit low angular momentum, just as we discovered in our four local high- z analogs?

Measuring the angular momentum in disks at $z \approx 2$ is extremely difficult, as their inner rotation structure ($< 0''.1$) is hard to resolve and their outer parts, holding most of the angular momentum, have low surface brightness (owing to the $\sim (1+z)^{-4}$ cosmological dimming). However, a generic theoretical expectation in Λ CDM cosmology is that the mean relation between mass and angular momentum changes with time, due to cosmic expansion. To first order, this can be seen in the model of a spherical halo (virial mass M_h , radius R_h , velocity V_h , angular momentum J_h). Following Mo et al. (1998), the specific angular momentum $j_h \equiv J_h/M_h = \sqrt{2}\lambda R V$ can be expressed as

$$j_h = 2^{2/3} G^{2/3} \lambda M_h^{2/3} H(z)^{-1/3} \Delta_c(z)^{-1/6}, \quad (4)$$

where G is the gravitational constant. The spin parameter λ , here defined as in Bullock et al. 2001, is approximately independent of z (Hetzner & Burkert 2006). The Hubble parameter varies as $H(z) = H_0 E(z)$,

where H_0 is the local Hubble constant and $E(z) = (\Omega_m(1+z)^3 + \Omega_\Lambda)^{1/2}$ in a flat universe. The function $\Delta_c(z)$ is the over-density factor of the virialized halo relative to the mean density of the universe, approximated analytically as (Bryan & Norman 1998)

$$\Delta_c(z) = 18\pi^2 - 82\Omega_\Lambda E^{-2}(z) - 39\Omega_\Lambda^2 E^{-4}(z). \quad (5)$$

Substituting these analytical expressions for $H(z)$ and $\Delta_c(z)$ into Equation (4) yields $j_h \propto M_h^{2/3} (1+z)^{-1/2}$, where the z -dependence is an approximation. Assuming a z -independent M_s/M_h (as verified to $z \lesssim 4$, Behroozi et al. 2013) and retention of the baryon specific angular momentum during disk formation (Fall & Efstathiou 1980), a similar z -scaling applies to j_s ,

$$j_s \propto M_s^{2/3} (1+z)^{-1/2}. \quad (6)$$

Modern hydrodynamic galaxy simulations in a cosmological context, the Magneticum Pathfinder (Hirschmann et al. 2014) and Illustris (Vogelsberger et al. 2014) simulations, produce robust angular momentum statistics (Genel & et al. 2015; Teklu & et al. 2015). Both approximately confirm the z -scaling of Equation (6) for star-forming M_s^* -disks (priv. comm. S. Genel and A. Teklu).

In summary, there is strong theoretical indication that the population of M_s^* -disks at $z \approx 2$ has lower j_s (by a factor ~ 2) than the mass-matched disk population at $z \approx 0$. The expected j_s values of the high- z disks are consistent with those measured in our local analogs within the uncertainties (at 1.3 standard deviations). Following the stability discussion of Section 3.1, low angular momentum must then play a major role in making the high- z star-forming disks semi-stable. It thus seems that the cosmic growth of angular momentum is a dominant driver behind the evolution of the population of star-forming M_s^* -galaxies from semi-stable, turbulent, clumpy to stable, flat, regular spiral disks. We emphasize that this conclusion applies to the evolution of the *population* of M_s^* -galaxies, not individual galaxies. A M_s^* -galaxy at $z \approx 2$ does not normally evolve into a M_s^* -galaxy at $z \approx 0$, but into a much more massive object (van Dokkum et al. 2013) such as an ETG; nor are individual disks expected to follow $j_s \propto (1+z)^{-1/2}$.

A potential caveat is that typical $z \approx 2$ disks of stellar mass near M_s^* may have even higher gas fractions ($\sim 50\%$, Carilli & Walter 2013) than our objects, which would contribute an extra stability factor of 40%. However, this is still sub-dominant to the change in j , and may arise from it.

4. CONCLUSIONS

This article reports the detection of exceptionally low angular momentum in four rare examples of clumpy, turbulent star-forming galaxies at $z \approx 0.1$. The low angular momenta offer a powerful new explanation for their marginal stability, enabling large clumps to form and pristine gas to convert rapidly into stars. The key to obtaining robust measurements of specific angular momentum is the combination of IFS data with high spatial resolution in the galaxy centers (from Keck-OSIRIS) and high surface brightness sensitivity out to large radii (from Gemini-GMOS).

The circumstances through which clumpy low- j disks with high gas fractions can exist in the local Universe

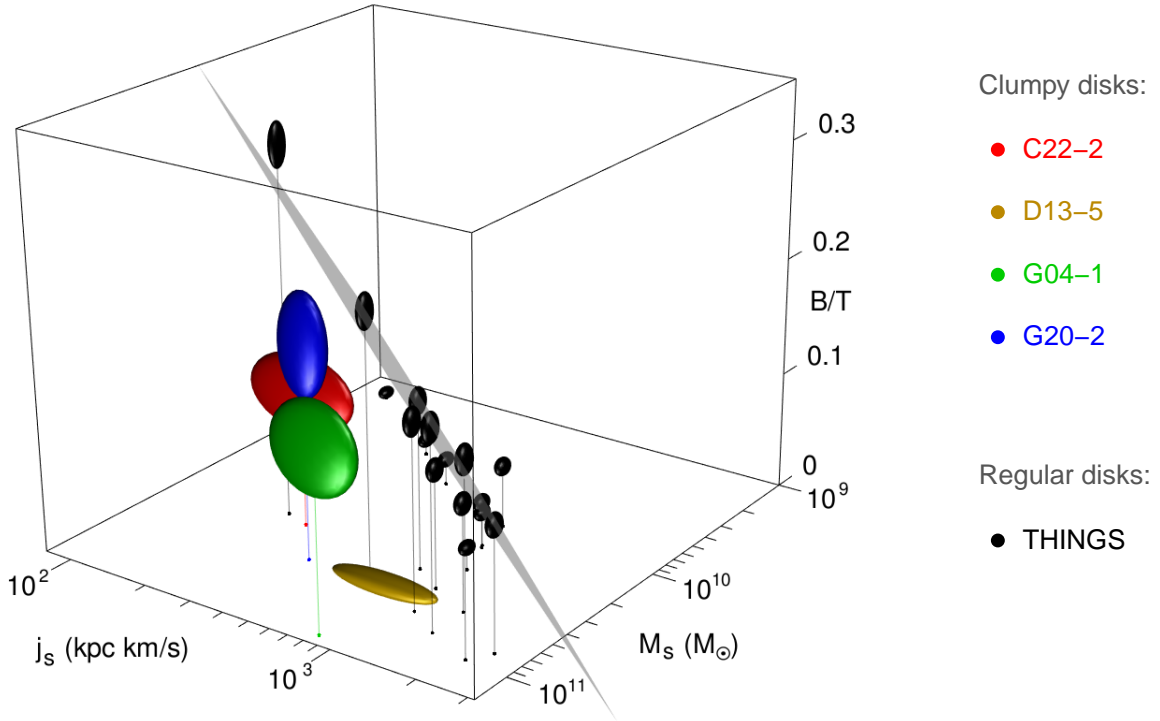


Figure 2. [Interactive 3D-figure in Adobe PDF Viewer. Feel free to use the standalone and animated versions in our Dropbox.] Mass-spin-morphology space. Dark points represent the 16 typical local spiral galaxies of the THINGS sample (Obreschkow & Glazebrook 2014; Walter et al. 2008); colored points are the four clumpy disks of this study – they appear to be deficient in angular momentum j_s . Ellipsoids represent 1σ -statistical uncertainties. The j_s -values of the DYNAMO objects are the best estimates $j_{s,\text{tot}}$ (see Appendix B) listed in Table 1. The grey plane is best fits to the data accounting for the 3D Gaussian uncertainties.

remain to be explored, but whatever the origin of these objects, it is likely that the physical mechanisms driving clump formation and turbulence are the same as at $z \approx 2$ and independent of the galaxies’ origin. By exploiting the analogy between our targets and *typical* star-forming galaxies at $z \approx 2$, we find evidence that low angular momentum is also a dominant cause of the low stability of such high- z galaxies. Hence, a change in angular momentum, driven by cosmic expansion, appears to be the primary cause for the remarkable difference between clumpy M_s^* -disks at high z (which likely evolve into ETGs) and mass-matched local spirals.

We dedicate this publication to the memory Prof Peter McGregor, who passed away during this work. We are indebted to him for his outstanding contributions to astrophysics, his leadership of Integral Field Spectroscopy in Australia and his inspiration to the DYNAMO project.

Acknowledgements: Based on observations made with the NASA/ESA Hubble Space Telescope, obtained at the Space Telescope Science Institute, which is operated by the Association

of Universities for Research in Astronomy, Inc., under NASA contract NAS 5-26555. These observations are associated with program #12977. — We acknowledge observational support from the Swinburne Keck Time Assignment Committee, and financial support from ARC Discovery Project DP130101460. This work is also based on observations obtained at the Gemini Observatory (programs GN-2011B-Q-54 and GS-2011B-Q-88), which is operated by the Association of Universities for Research in Astronomy, Inc., under a cooperative agreement with the NSF on behalf of the Gemini partnership: the National Science Foundation (United States), the National Research Council (Canada), CONICYT (Chile), the Australian Research Council (Australia), Ministério da Ciência, Tecnologia e Inovação (Brazil) and Ministerio de Ciencia, Tecnología e Innovación Productiva (Argentina). R.B. acknowledges support from the Victorian Department of State Development, Business and Innovation through the Victorian International Research Scholarship (VIRS). — Some of the data presented herein were obtained at the W.M. Keck Observatory, which is operated as a scientific partnership among the California Institute of Technology, the University of California and NASA. The Observatory was made possible by the generous financial support of the W.M. Keck Foundation. The authors wish to recognize and acknowledge the very significant cultural role and reverence that the summit of Mauna Kea has always had within the indigenous Hawaiian community.

APPENDIX

A. IFS data and pre-processing

We observed all four targets with the Keck-OSIRIS integral field spectrograph in Adaptive Optics (AO) mode to obtain spectra around the Pa α (1875 nm rest-frame) line in $5''.2 \times 6''.7$ fields. The spatial resolution is $0''.24$ full-width-half-maximum (FWHM) of the point spread function (PSF), corresponding to the sub-kpc resolutions listed in Table 1. For the two more distant galaxies (G04-1 and G20-2) we also obtained deeper IFS data around the H β (486.1 nm rest-frame) line using the Gemini-GMOS at a natural seeing of $0''.5$ in three fields (one for G04-1, two for G20-2, visible as 45° rotated rectangles in Figure 1).

The 3D-data cubes (two spatial dimensions, one wavelength dimension) from OSIRIS and GMOS were converted into rest-frame line-of-sight velocity maps $v'(\mathbf{x})$ (from Pa α , H β) and background-subtracted continuum flux maps $\Sigma_s(\mathbf{x})$, on a discrete cartesian grid $\mathbf{x}_i = (x_i, y_i)$ with $0''.1 \times 0''.1$ pixels. We assume the stellar surface density to be proportional to $\Sigma_s(\mathbf{x})$ (hence the subscript). We combine the OSIRIS and GMOS data (for G04-1 and G20-2) by registering the maps at $0''.1$ -pixel accuracy, which suffices given the $0''.5$ PSF of GMOS. The GMOS continuum values are scaled to match the OSIRIS continuum at the edge of the OSIRIS maps. Merged continuum and velocity maps are then created by taking OSIRIS data where available and GMOS data otherwise. In this way, the central parts, where spatial resolution is critical, always come from OSIRIS.

B. Kinematic fits and angular momentum measurement

The surface density maps $\Sigma_s(\mathbf{x})$ and line-of-sight velocity maps $v'(\mathbf{x})$ on a discrete grid of $0''.1$ -pixels $\mathbf{x}_i = (x_i, y_i)$ are fitted with a disk model using a customised algorithm:

1. Fit galaxy centre $\mathbf{x}_0 = (x_0, y_0)$ by minimizing the convolution of the density-weighted velocity map $w = \Sigma_s v'$ and its mirror image, $\int d^2x w(\mathbf{x} - \mathbf{x}_0)w(\mathbf{x}_0 - \mathbf{x})$. This method is exact for axially symmetric objects.
2. Fit inclination η and position angle α , which set the projection factor $f_{\eta,\alpha}(\mathbf{x}) = (\cos^2\varphi + \sin^2\varphi \cos^{-2}\eta)^{1/2}$, $\varphi = \arg(\mathbf{x} - \mathbf{x}_0) - \alpha$, such that the radius in the galaxy plane is $r = f_{\eta,\alpha}(\mathbf{x})|\mathbf{x} - \mathbf{x}_0|$, and the factor $g_{\eta,\alpha}(\mathbf{x}) = f_{\eta,\alpha}(\mathbf{x})(\cos\varphi \sin\eta)^{-1}$, such that the circular velocity is $v(r) = g_{\eta,\alpha}(\mathbf{x})v'(\mathbf{x})$. The parameters η and α are fitted simultaneously without assuming a rotation or density structure other than a flat, axial disk. This fit is performed by minimizing the RMS of the uncertainty-weighted Σ_s and v residuals in circular rings in the galaxy plane. We do not account for beam-smearing in the velocity field, since the central steep parts of the rotation curve are sampled with adaptive optics in all four targets. Explicitly, the maximal relative velocity change per PSF FWHM Δx , calculated as $\max\{\nabla v'(\mathbf{x})\}\Delta x v_{\text{flat}}^{-1}$, is much smaller than unity in all cases.
3. Fit a four-parameter disk+bulge density profile $\Sigma_{\text{model},s}(r) = \Sigma_d \exp(-r/r_d) + \Sigma_b \exp(-r/r_b)$ to Σ_s using a maximum likelihood estimation. Adopting alternative bulge profiles, e.g. with variable Sérsic index, makes little difference to the quality of these fits and has negligible impact on j_s . In the fitting procedure, the model $\Sigma_{\text{model},s}$ is blurred by the PSF, which depends on \mathbf{x} due to the combination of adaptive optics and natural seeing.
4. Fit a two-parameter velocity profile (Boissier et al. 2003) $v_{\text{model}}(r) = v_{\text{flat}}(1 - \exp[-r/r_{\text{flat}}])$ to $v(r)$ using a maximum likelihood estimation.

Using only the first two fitting steps, we compute the directly observed stellar specific angular momentum as

$$j_{s,\text{obs}} = \left[\sum_i \Sigma_{s,i} \right]^{-1} \sum_i \Sigma_{s,i} r_i v_i, \quad (1)$$

where i goes over all pixels with velocity and continuum data, r_i is the radius in the disk plane and v_i is the circular velocity. So far, we only assumed the stellar mass density to be proportional to Σ_s ; the proportionality factor turns out to be irrelevant for $j_{s,\text{obs}}$ as it cancels out in Equation (1). For the same reason, there is no need to correct Σ_s by an inclination factor $\cos^{-1}\eta$. The values $j_{s,\text{obs}}$ are not converged in the sense that they would increase if data at larger radii were available. To obtain the best estimates of the full j_s , called $j_{s,\text{tot}}$, we extend the sums in Equation (1) to the domain \mathbb{R}^2 (to infinite r). Where measurements for Σ_s or v are unavailable, their values are approximated by $\Sigma_{\text{model},s}$ and v_{model} , respectively.

The best-fit parameters of our targets are listed in Table 1. For C22-2, r_{flat} and v_{flat} are individually almost unconstrained, however, their product is constrained at the 15% level, such that the rotation curve is well constrained at the radii that most strongly contribute to the angular momentum. We estimate the uncertainties of $j_{s,\text{tot}}$ by propagating the covariance matrix of the fits, taken as the inverse Hessian of the log-likelihood function. For the two galaxies with both GMOS and OSIRIS data (G04-1, G20-2), we verified that the extrapolations based solely on OSIRIS data ($j_{s,\text{tot}} = 958 \pm 18\%$, $397 \pm 13\%$) are consistent with the more accurate extrapolations from combined OSIRIS+GMOS data ($j_{s,\text{tot}} = 834 \pm 14\%$, $394 \pm 8\%$).

C. Tests of the fitting algorithm

We tested the fitting procedure described in Appendix B against 10^3 mock datasets of model-galaxies, as illustrated in Figure 3. The quality of these mock data is similar to the quality of our targets with OSIRIS+GMOS data. We found that our model recovers the true total specific angular momentum $j_{s,\text{tot}}$ at an accuracy of $\sim 5\%$ with negligible systematics. Note that the estimated statistical uncertainties of $j_{s,\text{tot}}$ in Table 1 are generally larger than 5%, because the galaxies are not perfectly axially symmetric disks; hence the fits and extrapolations are somewhat less certain.

We also checked the algorithm on the galaxy NGC 3198, a regular M_s^* -disk for which kinematic fits (Leroy et al. 2008) and j_s -measurements (Obreschkow & Glazebrook 2014) were performed independently at high precision using kinematic data reaching out to ~ 10 exponential radii. For the present test, the data were heavily truncated and smoothed (see Figure 4) to a physical size and resolution similar to the IFS data of the four targets. Applying our fitting algorithm to this degraded version of NGC 3198 produces results in close agreement with those drawn from the reference work (Leroy et al. 2008; Obreschkow & Glazebrook 2014) (bottom of Table 1).

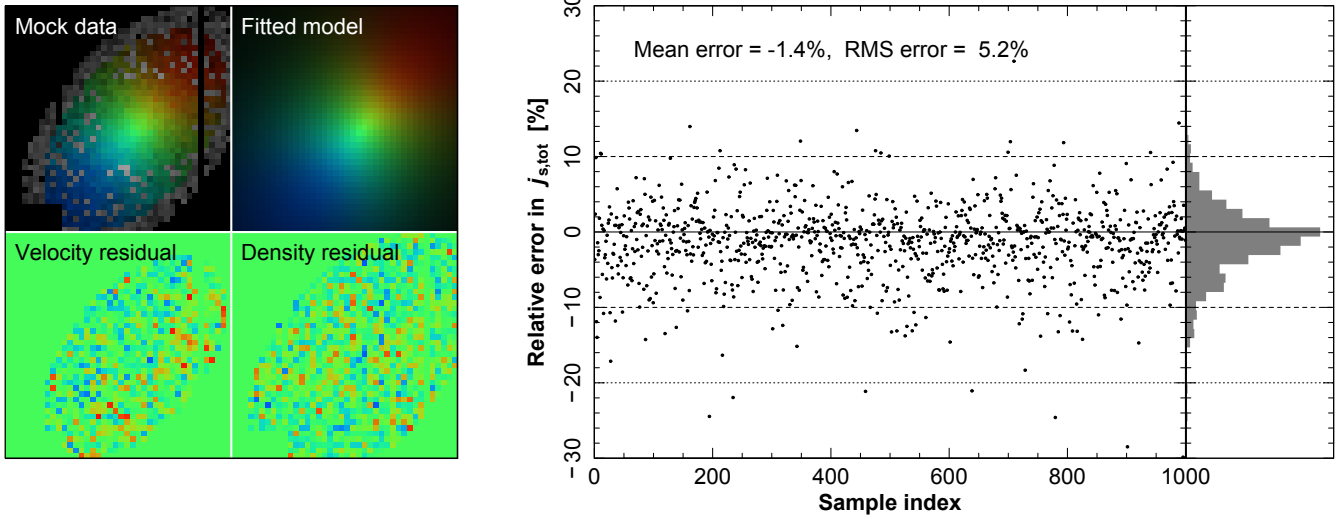


Figure 3. LEFT: example of a mock dataset and the corresponding fits with residuals. The mock data represent an inclined model-galaxy with exponential surface density profile and differential rotation. The data has been degraded in three ways: (1) it is blurred to a physical scale corresponding to the Keck-OSIRIS PSF, (2) signal in some region has been removed (grey and black regions) to mimic sensitivity limitations and sensor errors, and (3) Gaussian noise of realistic amplitude has been added. The colorscales are as in Figure 1. RIGHT: Relative difference between the recovered value of the total specific angular momentum $j_{s,\text{tot}}$ and the input value in 10^3 random mock dataset, similar to the one shown in the left panel.

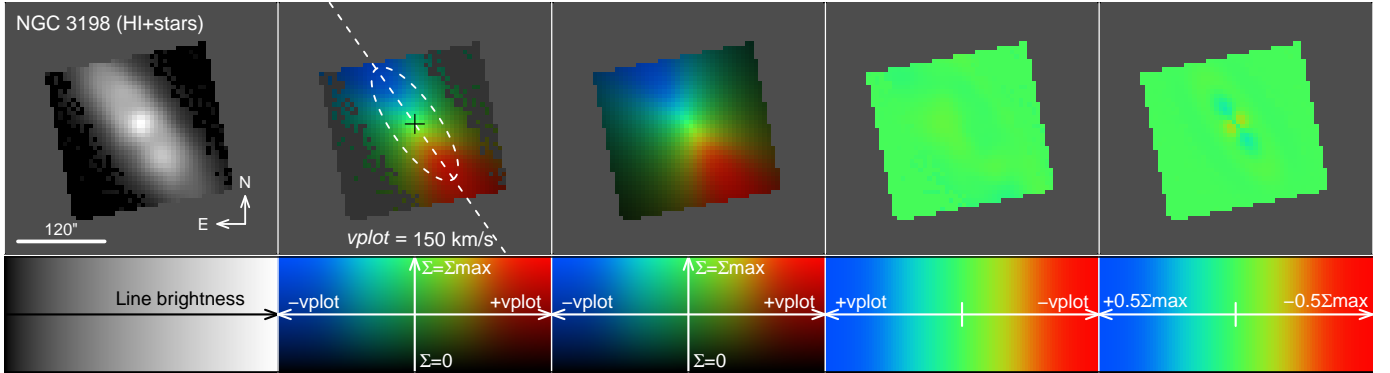


Figure 4. Same as Figure 1, but for the heavily degraded local control galaxy NGC 3198 (see Appendix C).

REFERENCES

- Andersen D. R., Bershadsky M. A., Sparke L. S., Gallagher III J. S., Wilcots E. M., van Driel W., Monnier-Ragaine D., 2006, *ApJS*, 166, 505
- Bassett R., et al., 2014, *MNRAS*, 442, 3206
- Behroozi P. S., Wechsler R. H., Conroy C., 2013, *ApJ*, 770, 57
- Bell E. F., McIntosh D. H., Katz N., Weinberg M. D., 2003, *ApJS*, 149, 289
- Boissier S., Prantzos N., Boselli A., Gavazzi G., 2003, *MNRAS*, 346, 1215
- Bournaud F., Elmegreen B. G., Elmegreen D. M., 2007, *ApJ*, 670, 237
- Bryan G. L., Norman M. L., 1998, *ApJ*, 495, 80
- Bullock J. S., Kolatt T. S., Sigad Y., Somerville R. S., Kravtsov A. V., Klypin A. A., Primack J. R., Dekel A., 2001, *MNRAS*, 321, 559
- Carilli C. L., Walter F., 2013, *ARA&A*, 51, 105
- Dekel A., et al., 2009, *Nature*, 457, 451
- Elmegreen B. G., Elmegreen D. M., 2005, *ApJ*, 627, 632
- Elmegreen B. G., Elmegreen D. M., Sánchez Almeida J., Muñoz-Tuñón C., Dewberry J., Putko J., Teich Y., Popinchalk M., 2013, *ApJ*, 774, 86
- Fall S. M., Efstathiou G., 1980, *MNRAS*, 193, 189
- Fall S. M., Romanowsky A. J., 2013, *ApJ*, 769, L26
- Fisher D. B., et al., 2014, *ApJ*, 790, L30
- Förster Schreiber N. M., et al., 2006, *ApJ*, 645, 1062
- Genel S., et al., 2015, *ArXiv e-prints*
- Genzel R., et al., 2008, *ApJ*, 687, 59
- Glazebrook K., 2013, *Publications of the Astronomical Society of Australia*, 30, 56
- Glazebrook K., Peacock J. A., Miller L., Collins C. A., 1995, *MNRAS*, 275, 169
- Green A. W., et al., 2014, *MNRAS*, 437, 1070
- Hetznecker H., Burkert A., 2006, *MNRAS*, 370, 1905
- Hirschmann M., Dolag K., Saro A., Bachmann L., Borgani S., Burkert A., 2014, *MNRAS*, 442, 2304
- Karim A., et al., 2011, *ApJ*, 730, 61
- Kormendy J., Fisher D. B., 2008, in *Astronomical Society of the Pacific Conference Series*, Vol. 396, *Formation and Evolution of Galaxy Disks*, Funes J. G., Corsini E. M., eds., p. 297
- Kroupa P., 2001, *MNRAS*, 322, 231
- Leroy A. K., Walter F., Brinks E., Bigiel F., de Blok W. J. G., Madore B., Thornley M. D., 2008, *AJ*, 136, 2782
- McMillan P. J., 2011, *MNRAS*, 414, 2446
- Mo H. J., Mao S., White S. D. M., 1998, *MNRAS*, 295, 319
- Murray N., 2011, *ApJ*, 729, 133
- Muzzin A., et al., 2013, *ApJ*, 777, 18
- Obreschkow D., Glazebrook K., 2014, *Astrophys. J.*, 784, 26
- Obreschkow D., Rawlings S., 2009, *ApJ*, 696, L129

- Peng Q.-H., 2001, in *Astronomical Society of the Pacific Conference Series*, Vol. 230, *Galaxy Disks and Disk Galaxies*, Funes J. G., Corsini E. M., eds., pp. 225–228
- Robotham A. S. G., Obreschkow D., 2015, *ArXiv e-prints*
- Rodighiero G., et al., 2011, *ApJ*, 739, L40
- Romanowsky A. J., Fall S. M., 2012, *ApJS*, 203, 17
- Romeo A. B., Wiegert J., 2011, *MNRAS*, 416, 1191
- Tacchella S., et al., 2015, *Science*, 348, 314
- Tacconi L. J., et al., 2010, *Nature*, 463, 781
- Teklu A. F., et al., 2015, *ArXiv e-prints*
- Toomre A., 1964, *ApJ*, 139, 1217
- van Dokkum P. G., et al., 2013, *ApJ*, 771, L35
- Vogelsberger M., et al., 2014, *MNRAS*, 444, 1518
- Walter F., Brinks E., de Blok W. J. G., Bigiel F., Kennicutt R. C., Thornley M. D., Leroy A., 2008, *AJ*, 136, 2563
- Wang B., Silk J., 1994, *ApJ*, 427, 759
- Westfall K. B., Andersen D. R., Bershadsky M. A., Martinsson T. P. K., Swaters R. A., Verheijen M. A. W., 2014, *ApJ*, 785, 43
- York D. G., et al., 2000, *AJ*, 120, 1579